JGR Space Physics

RESEARCH ARTICLE

10.1029/2020JA028432

Electron Density Depletion Region Observed in the Polar Cap Ionosphere

L. M. Bjoland[1,2], Y. Ogawa[3], U. P. Løvhaug[4], D. A. Lorentzen[1,2], S. M. Hatch[2], and K. Oksavik[1,2]

[1]Arctic Geophysics Department, The University Centre in Svalbard, Longyearbyen, Norway, [2]Birkeland Centre of Space Science, University of Bergen, Bergen, Hordaland, Norway, [3]National Institute of Polar Research, Tokyo, Japan, [4]University of Tromsø—The Arctic University of Norway, Tromsø, Norway

Key Points:

- An early morning electron density depletion region is observed by the EISCAT Svalbard radar in the *F*-region polar cap ionosphere
- This depletion region is most pronounced during winter and equinox when the solar activity is moderate or high
- Results indicate that the formation of the depletion region is connected to ion frictional heating

Correspondence to:

L. M. Bjoland,
lindisb@unis.no

Citation:

Bjoland, L. M., Ogawa, Y., Løvhaug, U. P., Lorentzen, D. A., Hatch, S. M., & Oksavik, K. (2021). Electron density depletion region observed in the polar cap ionosphere. *Journal of Geophysical Research: Space Physics*, *126*, e2020JA028432. https://doi.org/10.1029/2020JA028432

Received 2 JUL 2020
Accepted 20 NOV 2020

Abstract This paper presents and discusses electron density depletion regions observed with the incoherent scatter EISCAT Svalbard Radar (ESR) located at 75.43°N geomagnetic latitude. The data include several decades of measurements, which make them suitable for studying statistical features and characteristics of the ionospheric parameters. Here we focus on the electron density depletions and their dependence on diurnal and seasonal variations and solar activity. An electron density depletion region is identified in the ESR data in the early morning sector. This depletion region seems to be clearest during equinox and winter and moderate/high solar activity. An enhancement in the ion temperature is often co-located with the electron density depletion region. The ion temperature enhancement could indicate that ion frictional heating is related to the electron density depletion region. However, during summer when the solar activity is low, the electron density depletion is not observed although the ion temperature is enhanced, suggesting that formation of the electron density depletion regions due to ion frictional heating may depend on the background effective temperature and O/N_2 ratio. In addition, seasonal changes in the solar zenith angle could also contribute to the formation of the depletion region.

1. Introduction

Structures of depleted electron density in the high-latitude ionosphere can be caused by several different processes including changes in the convection pattern and changes in the recombination rates. These depletion regions are typically classified according to size, shape and formation mechanism. Among the different types of depletion regions are the high-latitude troughs (e.g., Jones et al., 1990), polar holes (Brinton et al., 1978), and auroral cavities (Doe et al., 1993). In the present study the EISCAT Svalbard Radar (ESR) is used to investigate statistical structures of reduced electron density in the *F*-region ionosphere above Svalbard. Due to strong coupling to the solar wind, the high-latitude ionosphere is highly variable. An improved understanding of plasma structures such as depletion regions is important for understanding the coupled magnetosphere-ionosphere system.

One example of a type of plasma depletion structure is the ionospheric trough, which is typically classified as either "high-latitude" or "mid-latitude" troughs based on location. Troughs are a few degrees wide in latitude, but have an elongated shape in the longitudinal direction. The main formation mechanism is thought to be different for high-latitude and mid-latitude troughs: While the mid-latitude trough usually is formed due to prolonged recombination of ionospheric plasma when a stagnation region in the convection pattern is located in darkness, high-latitude troughs are typically connected to frictional heating and can form when there is a large difference between the ion and neutral velocities (e.g., Jones et al., 1990). In the *F*-region O^+ chemical loss occurs through a two-step process, with charge exchange followed rapidly by recombination. An increase in the ion temperatures leads to enhanced O^+ recombination rates and, as a consequence, also an increase in the dissociative recombination process (e.g., Rodger et al., 1992; Schunk et al., 1976). The following charge exchange reactions are important:

$$O^+ + O_2 \rightarrow O_2^+ + O$$
$$O^+ + N_2 \rightarrow NO^+ + N$$
$$N_2^+ + O \rightarrow NO^+ + N$$
$$N_2^+ + O_2 \rightarrow N_2 + O_2^+$$

NO^+ and O_2^+ then recombine with electrons to create neutral oxygen and nitrogen. Frictional heating also causes upflow of neutral nitrogen and oxygen from lower altitudes into the *F* region. The resulting enhanced concentrations of oxygen and nitrogen contribute to an increased recombination rate (e.g., Williams & Jain, 1986; Winser et al., 1986).

Although high-latitude troughs have not been as extensively studied as mid-latitude troughs, some important investigations have been carried out. Early studies of high-latitude troughs were reviewed by Rodger et al. (1992). In more recent years, Ma et al. (2000) investigated a case where a trough occurred close to the dayside polar cap boundary during the recovery of a geomagnetic storm. Zou et al. (2013) studied the electrodynamics of an observed high-latitude trough and found that the trough was colocated with a downward field-aligned current. Vanhamäki et al. (2016) suggest that downward field-aligned currents are the initial cause of troughs, which are further depleted when they move southward into the westward electrojet due to the enhanced ion temperatures there. Voiculescu et al. (2016) also suggest a two-step formation mechanism in a study of the high-latitude post-midnight trough in summer. Energetic electron precipitation leads to an upward flow of molecular ions into the *F*-region. Initially, a trough will then form due to increased recombination caused by the enhanced concentrations of molecular ions. As the trough moves into a region of strong eastward flow, it will undergo further depletion due to frictional heating.

Polar holes and auroral cavities are two other examples of structures of depleted electron density that can occur at high latitudes. These differ from the described trough structure in size and shape, and while frictional heating is typically considered to be connected to the formation of high-latitude troughs, the formation of auroral cavities and polar holes are more often connected to field-aligned currents and prolonged recombination in darkness. Auroral cavities have a narrow shape and tend to be organized in the east-west direction, similar to the organization of large-scale field-aligned currents. These cavities are located on the nightside, poleward of the auroral oval. Typically, the width of the cavities is less than 100 km and the density is 20%–70% less than the surrounding background plasma (Doe et al., 1993). The formation of auroral cavities is connected to downward field aligned currents (e.g., Aikio et al., 2004; Doe et al., 1993). Polar holes are large-scale depletion regions, that were first observed by Brinton et al. (1978) in satellite data from the southern hemisphere. They occur on the nightside between 70° and 80° magnetic latitude, co-located with the auroral cavities (e.g., Benson & Grebowsky, 2001). During quiet geomagnetic conditions, polar holes form as a result of slow anti-sunward convection across the dark polar cap or circulation in perpetual darkness (Brinton et al., 1978; Jenner et al., 2020; Sojka et al., 1981). Circulation in perpetual darkness can occur during low geomagnetic activity when the polar cap is contracted, or in lobe cells when the interplanetary magnetic field (IMF) is northward.

In addition to structures of electron density depletion, the high-latitude ionosphere is also characterized by high-density structures such as polar cap patches (e.g., Buchau et al., 1983; Carlson et al., 2002) and auroral blobs (e.g., Kelley et al., 1982). Polar cap patches usually have sizes of 100–1,000 km, and are transported across the polar cap following the convection pattern (e.g., Buchau et al., 1983; Carlson et al., 2002; Oksavik et al., 2006, 2010). The region between patches may therefore be confused with a depletion region, but in reality represents the background ionospheric density between two density enhancements.

In this paper, we further investigate such electron density variations using the ESR and Swarm satellite measurements. The main purpose of the paper is to study structures of depleted electron density, or depletion regions, at high latitudes.

2. Data and Method

The ESR operates with a transmission frequency of 500 MHz and is located near Longyearbyen, Svalbard (geographic coordinates: 78.15°N, 16.02°E, geomagnetic coordinates: 75.43°N, 110.68°E). Range profiles of several primary plasma parameters are provided by the radar. In this study, we investigate the electron density and ion temperature at *F*-region altitudes between 200 and 500 km, using all available data from the beginning of ESR operations in 1996 until 2016. Typically, the ESR is operated for a few hours in campaign mode, meaning that the data are not continuous. However, by using the accumulated data, a sufficient amount of data is acquired to compute statistical averages of the typical behavior of the depletion regions. Thus, for various categories of season and solar activity, an average day has been found by calculating hourly means of all available ESR data belonging to that category. A depletion region is then defined to occur

when the electron density is more than one standard deviation lower than the diurnal mean of the average day.

An assumed ion mass is necessary to derive the ion temperature from the ion acoustic lines measured by incoherent scatter radars. In the transition region where the ion composition changes from molecular to atomic ions, the ion mass is highly variable and thus difficult to estimate (e.g., Blelly et al., 2010). Ion temperature estimates from between 150 and 250 km altitude are therefore less precise, and as a consequence, ion temperature data were only used for altitudes above 250 km in this study. The data were analyzed using 5-min integration intervals in the Grand Unified Incoherent Scatter Design and Analysis Package (GUISDAP) software (Lehtinen & Huuskonen, 1996). In order to ensure that the observations are from approximately the same geographic area, data were only used when the elevation angle of the radar beam was larger than 70°.

To remove erroneous data, several filtering criteria were implemented. Data were only used when the electron density was between $10^{10}\mathrm{m}^{-3}$ and $10^{12}\mathrm{m}^{-3}$. Above 300 km altitude data were removed when the electron density was lower than $3 \times 10^{10}\mathrm{m}^{-3}$. The altitude of the maximum electron density (h_mF2) in the F-region varies with season, time of day and solar activity (e.g., Vickers et al., 2014), but is normally located around 200–300 km altitude. Electron density profiles were removed when the electron density increased with altitude above the region were we expect the h_mF2 to be located; around 350 km altitude during solar maximum years (1998–2003 and 2011–2015) and around 300 km altitude during solar minimum years. Furthermore, data were removed when the electron density uncertainty calculated by GUISDAP exceeded 50%. In addition, data were only used when the estimated ion temperature was less than 2000 K, since high ion temperatures are associated with high geomagnetic activity. The upper electron density limit was set because electron densities larger than $10^{12}\mathrm{m}^{-3}$ are usually caused by geomagnetic storms, or by the radar beam hitting a hard target. Densities lower than $10^{10}\mathrm{m}^{-3}$ were filtered out because such low densities are difficult to measure by the EISCAT radars and thus have high uncertainties. The power of the received signal depends on the electron density, and low electron densities cause a low signal-to-noize ratio. At altitudes above 300 km the background noise level is higher, which made it necessary to set a stricter criteria for the lowest electron density. Profiles where the electron density increases above the typical h_mF2 region were removed as this is usually caused by noise.

Figure 1 illustrates the ESR data coverage. This figure shows the distribution of the ESR samples used at an altitude of 300 km with time of day on the horizontal axes and number of samples on the vertical axes. Each panel corresponds to one combination of solar activity level and seasons. The data are split into three different levels of solar activity; low solar activity when $F10.7$ index is less than 100 solar flux units (sfu), moderate solar activity when 100 sfu $\leq F10.7 <$ 150 sfu and high solar activity when $F10.7 \geq$ 150 sfu. Furthermore, three different seasonal categories were used: (i) summer, defined as the period from the beginning of May to the end of August; (ii) winter, defined as the period from the beginning of November to the end of February; and (iii) equinox, defined as all days during the months of March, April, September, or October. The figure shows that there are more data available during low solar activity than moderate and high, and that the least number of data samples is available for summer during high solar activity. The data availability is typically best in the time period from when the ESR is located in the cusp region (~9 UT) until local noon (11 UT).

For space-based observations, plasma density measurements made by the Challenging Mini-Satellite Payload (CHAMP) satellite (Reigber et al., 2006) and the original Swarm constellation (Friis-Christensen et al., 2008) were used. The former mission extended over a ~10-year period from July 15, 2000 to September 19, 2010, covering an altitude range from ~300–455 km in a near-polar orbit, and included the Plasma Langmuir Probe instrument that made plasma density measurements at a 15-s cadence (Rother et al., 2005; McNamara et al., 2007). The latter is an ongoing mission that began November 22, 2013. The two lower satellites, Swarm A and C, nominally cover the range of altitudes between 445 and 528 km; Swarm B covers altitudes between 500 and 545 km. The Swarm Electric Field Instrument (Buchert et al., 2015; Knudsen et al., 2017; Lomidze et al., 2018) aboard each Swarm satellite includes two dedicated Langmuir Probes (LPs) that measure plasma density and electron temperature at 2 Hz. The Lomidze et al. (2018) in-flight calibrations have been applied to the Swarm plasma density measurements, and to account for differences

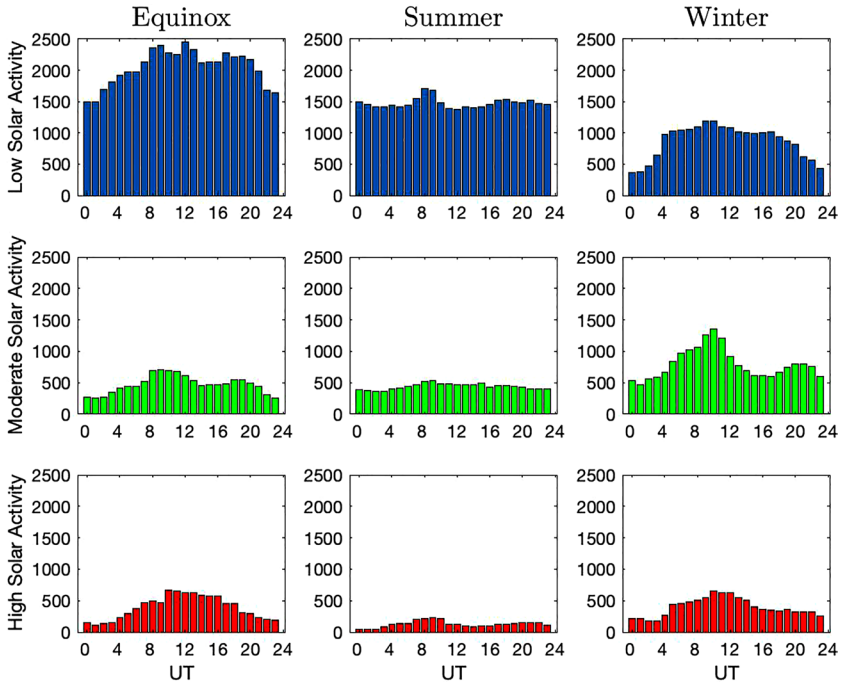

Figure 1. ESR data coverage at 300 km altitude as a function of time of day, season, and solar activity. UT time of day is along the horizontal axes, number of samples are shown on the vertical axes, rows correspond to different levels of solar activity, and columns represent different seasons.

in altitude the satellite measurements were scaled to a common altitude of 500 km via the methodology described by Hatch et al. (2020).

3. Results

Figure 2 shows averaged ESR electron density at altitudes between 200 and 480 km versus month of year. The three different subplots show the electron density for low, moderate and high solar activity, using the same three solar activity categories as in Figure 1. Approximately 60% of the ESR data correspond to "low solar activity category," 25% correspond to "moderate solar activity" and 15% correspond to "high solar activity." Only data from around local noon (10–12 UT) and for low geomagnetic activity (Kp ≤ 3) were used to make this figure. Bins with no data are shown in white.

Seasonal variations in the electron density, as seen in Figure 2, are mainly due to changes in the solar zenith angle and in the thermospheric composition. Changes in the solar zenith angle results in annual variations of the electron density with a maximum during summer. This can be seen in the ESR data for low solar activity. Changes in thermospheric composition is mainly controlled by the summer-to-winter meridional circulation with upwelling in the summer hemisphere and downwelling in the winter hemisphere. Upwelling leads to a lower O/N_2 ratio, while downwelling enhances the O/N_2 ratio. As a higher O/N_2 ratio results in a higher electron density, this means that the summer-to-winter meridional circulation increases the electron density in the winter hemisphere and decreases it in the summer hemisphere (Rishbeth, 1998). For moderate and high solar activity, the ESR data show semiannual variation in the electron density with the highest densities occurring near equinox. This type of semiannual variations could be the result of the combined effect of variations in the solar zenith angle and thermospheric composition (e.g., Millward et al., 1996; Zhang et al., 2005). Another contributing factor to the semiannual variations could be vertical ion drifts. Zhang et al. (2010) observed similar semiannual variations in the high-latitude *F* region electron density during the 2007 International Polar Year, and found that these variations were likely the result of stronger downward ion drift during summer which moves the ions into regions with higher recombination rates. Studies have shown that the difference between the

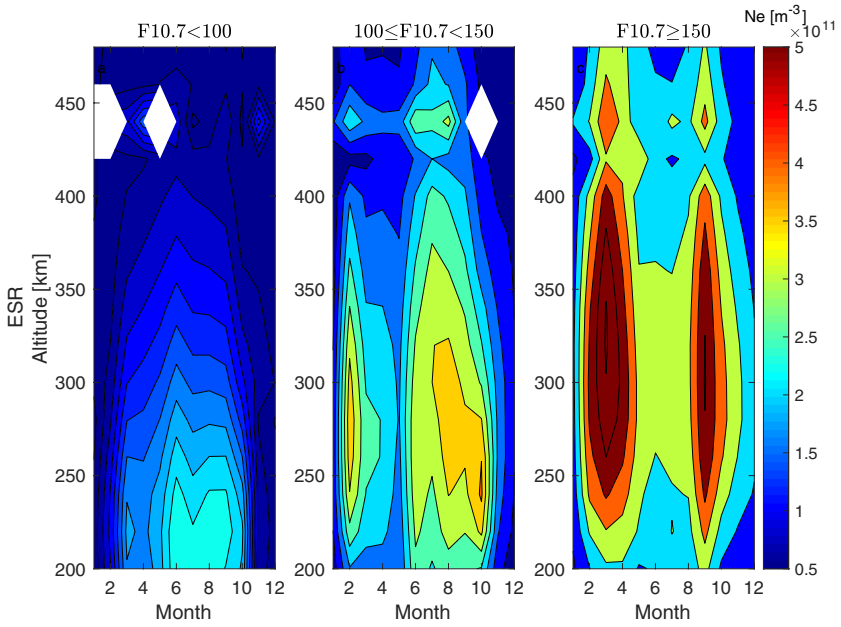

Figure 2. Contour plot of electron density from ESR for three different levels of solar activity. Altitudes from 200 to 480 km are given along the vertical axes, and month of year on the horizontal axes.

summer and winter O/N_2 ratio is larger during solar maximum (Burns et al., 2014), and that this is primarily due to an increase of the O/N_2 ratio in the winter hemisphere (Qian et al., 2016). Such solar activity dependence of the thermospheric composition might explain why a semiannual variation of the electron density is only seen for moderate and high solar activity in Figure 2. Similar semiannual variations were also seen in thermally excited 630.0 nm emissions using ESR measurements by Kwagala et al. (2018). They suggest that these variations could be due to the Russel-McPherron effect (Russell & McPherron, 1973). However, as data with Kp > 3 were removed when making Figure 2, it is unlikely that seasonal variations in geomagnetic activity could cause the equinoctial maxima seen in this figure. As expected, the electron density in Figure 2 is seen to increase with increasing solar activity. For higher solar activity, the areas of maximum electron density are also seen to extend over a larger altitude range.

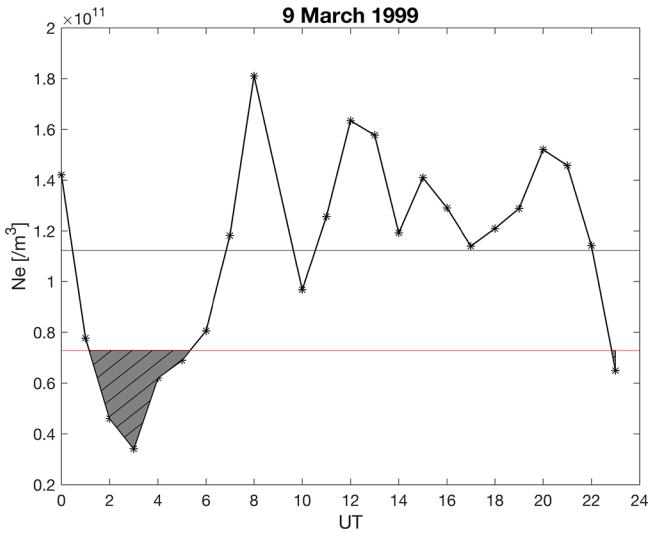

Figure 3. ESR electron density at 300 km altitude from March 9, 1999. The horizontal black line shows the diurnal mean. The red line indicates one standard deviation below the mean of the electron density. The hatched area below the red line marks where the electron density is less than one standard deviation below the mean.

An example of diurnal variations of electron density is displayed in Figure 3, which shows electron density as a function of UT for March 9, 1999 at an altitude of 300 km. The mean electron density is shown as a black line, and the red line indicates one standard deviation subtracted from the diurnal mean. The hatched area is where the electron density is less than one standard deviation below the mean. The electron density drops to less than one standard deviation below the mean around 1 UT and lasts until about 5 UT with a minimum at 3 UT. The electron density is also less than 1 standard deviation below the mean at 23 UT. Figure 4 shows all the EISCAT parameters for this day at altitudes between 80 and 680 km altitude to give a more complete overview of the conditions that day. The reduction in electron density for the time period ~1–5 UT, can be seen for all altitudes between ~230 and 500 km. Since ESR is operated in campaign-mode for only a few hours each day, data are usually not available for as long as for the day shown in Figures 3 and 4. By averaging over all the available ESR data, the data is still sufficient to study characteristics of the diurnal variations, and a diurnal mean and standard deviation below the mean can be calculated from the statistical average day similar to how it is done in this example for one day.

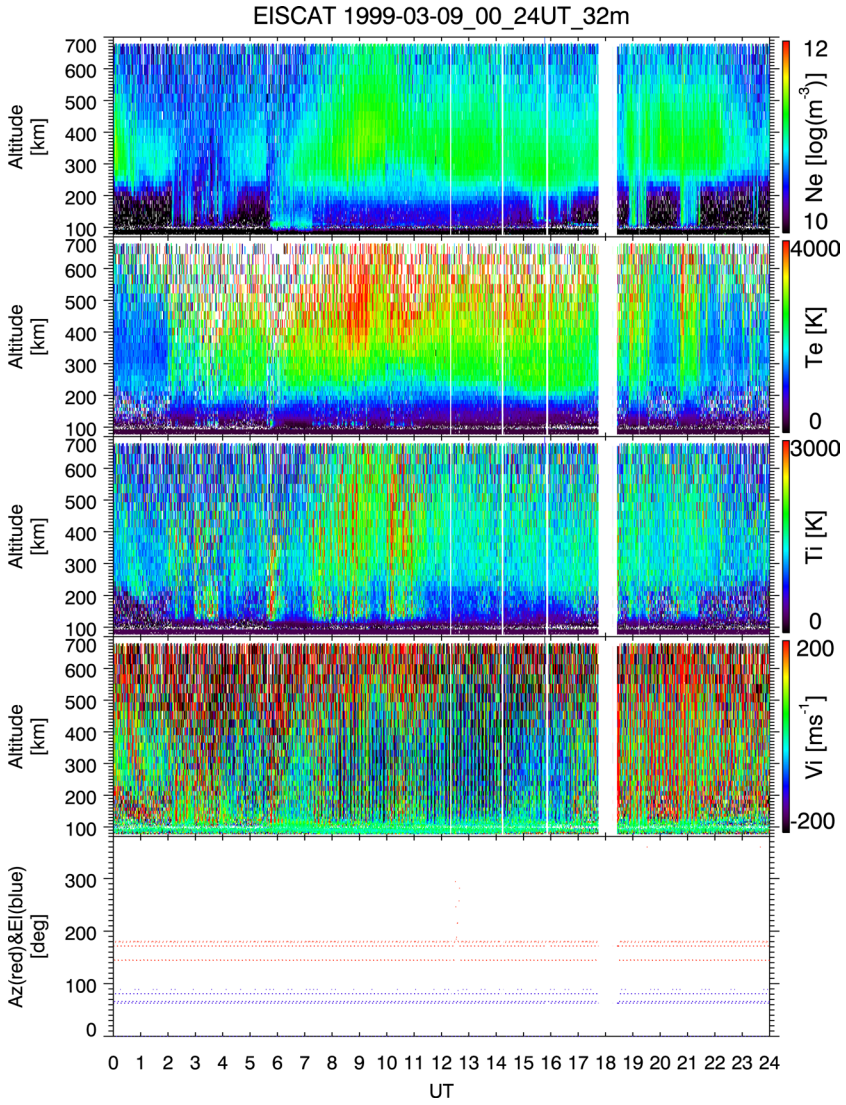

Figure 4. Color plot of EISCAT parameters from March 9, 1999. From top to bottom the panels show: electron density, electron temperature, ion temperature, ion velocity and azimuth and elevation of the radar beam.

In Figure 5 all the available ESR data from the equinoxes (March, April, September and October) have been used to study the average diurnal variation of electron density between 240 and 420 km altitude. The data have been separated into low solar activity (F10.7 < 100), shown in the left plot, moderate solar activity (100 ≤ F10.7 < 150) in the middle plot and high solar activity (F10.7 ≥ 150) shown in the right plot. It is clearly seen that the electron density is highest during daytime and when the solar activity is high. During low solar activity the electron density has a double hump structure with maxima around 9 UT in the morning and 16 UT in the afternoon. After 21 UT the electron density is clearly reduced, before it increases again in the morning from around 4 UT. This double hump structure is less evident for moderate and high solar activity. In addition to the diurnal variations, the electron density is further decreased during the early morning hours for moderate and high solar activity. The shift toward the morning sector for the electron density decrease is most clear for high solar activity and can be seen for all altitudes between 250 and 420 km from about midnight to 4 UT. In this time period the electron density above 300 km is much higher for high solar activity than for low or moderate. This is likely explained by plasma transport. Dayside electron density is higher during high solar activity. Furthermore, high solar activity could affect the cross-polar cap potential and lead to stronger convection. Thus, high solar activity is associated with increased plasma

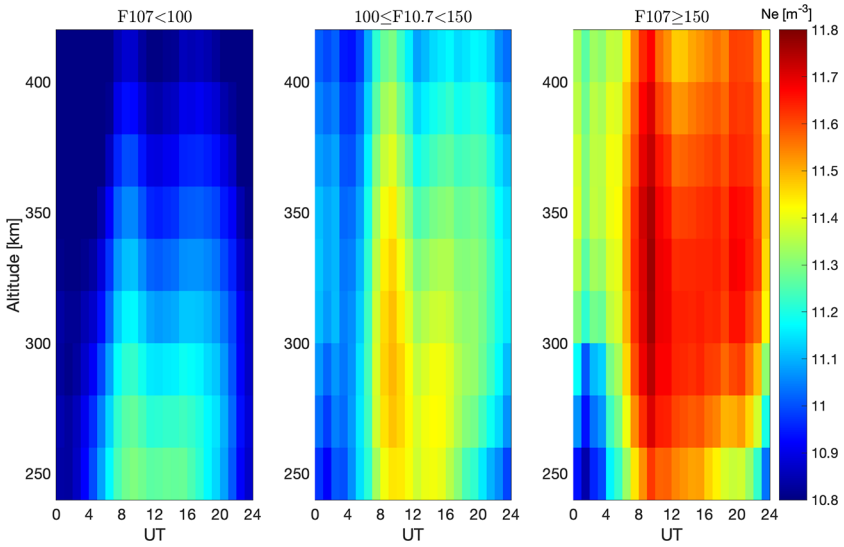

Figure 5. Color plots of ESR electron density during equinox at altitudes between 250 and 420 km versus time of day. Left panel: low solar activity. Middle panel: moderate solar activity. Right panel: high solar activity.

transport. Plasma transport plays a more important role at high altitudes where loss processes are slower. At these altitudes plasma can be transported across the polar cap and follow the convection pattern around on the morning side. For the high solar activity case the electron density depletion is therefore strongest below 300 km altitude. As the difference between magnetic local time (MLT) and UT in Longyearbyen is approximately 3 h, the time period from midnight to 4 UT corresponds to 3–7 MLT. Local solar time at Longyearbyen is approximately UT+1.

In Figure 6, seasonal and diurnal variations of the electron density and ion temperature at 300 km altitude during high, moderate and low solar activity are shown. The three panels correspond to equinox (panel a), summer (panel b) and winter (panel c). Each column shows the electron density and ion temperature during high (red line), moderate (green line) and low (blue line) solar activity. The standard errors are shown as error bars. As the number of samples in the ESR database is very large, the standard errors are very small although the highly dynamic high-latitude ionosphere lead to a high variance in the data set. The diurnal means for each of the seasonal/solar activity categories are shown as dashed lines, and solid lines represent one standard deviation below the mean. Depletion regions are marked as hatched areas in the figure. The double-humped diurnal variation in electron density observed in Figure 5 can be seen for all categories of solar activity during winter and equinox. For high solar activity, the electron density shows a clear depletion during the early morning hours (around 0–5 UT) for all seasons. This depletion region can also be seen for moderate solar activity during winter and equinox. In summer the depletion region during moderate activity is considerably shorter and lasts over ∼2–4 UT. During low solar activity the early morning depletion region does not appear at all in the summer season, but appears over ∼23–3 UT during winter and over ∼22–4 UT during equinox. In the summer case a small depletion region also appears during ∼21–23 UT, but this depletion does not last until the morning sector. Comparison of the electron density (top panels) with the ion temperature (bottom panels) indicates that an increase in the ion temperature typically also occurs during the early morning hours. This early morning increase in ion temperature is also visible for low solar activity during summer, although an electron density depletion region is not observed in this case. It is also interesting to note that for low solar activity there is a minimum in the ion temperature during 8–9 UT during summer and equinox. This minimum occurs over the same period as the peak electron density.

To validate the observations of the depletion region, the ESR results were compared with space-based observations. Figure 7 shows depletion regions calculated from density measurements within a 10-degree radius around the ESR radar, made by the CHAMP and Swarm satellites. These satellite measurements have been scaled to 500 km altitude. Figure 7 is divided into the same seasonal and solar activity categories as Figure 6 and the two figures in general show the same electron density variations. In particular, the satellite

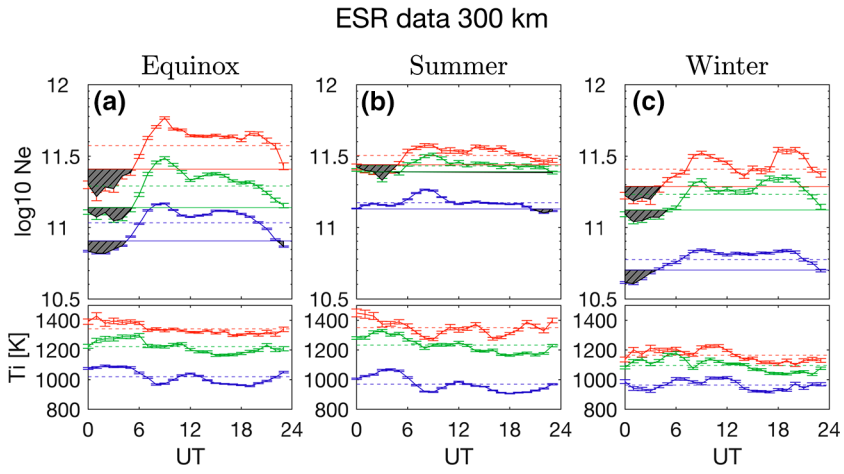

Figure 6. Plots of ESR electron density and ion temperature at 300 km altitude versus time of day. The columns show, from left to right, equinox, summer and winter. Each panel shows ESR electron density (top part) and ion temperature (bottom part) for both high (red line), moderate (green line) and low (blue line) solar activity. Depletion regions are shown as hatched areas.

measurements confirm the existence of the early morning depletion region. The most notable difference is perhaps that the electron density depletion region in the satellite measurements starts in the late evening. Differences between Figures 6 and 7 could be due to satellite measurements covering a larger spatial area and to differences in altitude between satellite and radar measurements.

To get a better understanding of the electron density distribution in the Northern Hemisphere, CHAMP and Swarm satellite measurements were further used to produce relative electron density maps. Figure 8 shows relative density statistics calculated from all CHAMP and Swarm density measurements made above 60° magnetic latitude in Modified Apex coordinates, with a reference altitude of 110 km (Laundal & Richmond, 2016; Richmond, 1995). Bins in each panel show the difference between the mean density in that bin and the mean of all bins, normalized by the mean of all bins. The circle, right triangle, square, and left triangle respectively denote the location of the EISCAT Svalbard radar at 0, 6, 12, and 18 UT.

Figure 8 shows that the early morning depletion region observed in ESR data is part of a larger area where the density is lower than the mean. This reduction in electron density is typically stronger and lasts longer at lower latitudes. Especially for winter and equinox, the lower densities on the nightside and higher densities

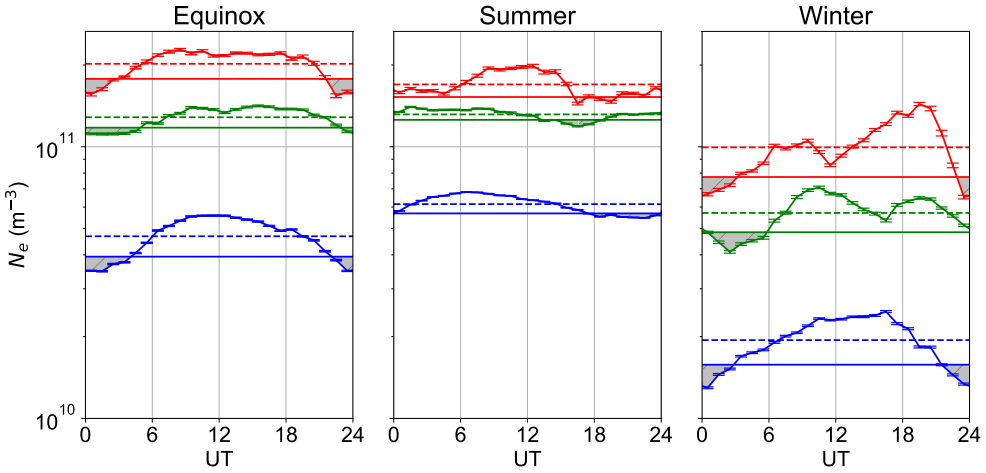

Figure 7. Plots of CHAMP/Swarm electron density scaled to an altitude of 500 km. Each panel shows CHAMP/Swarm electron density for both high (red line), moderate (green line) and low (blue line) solar activity. Depletion regions are shown as hatched areas.

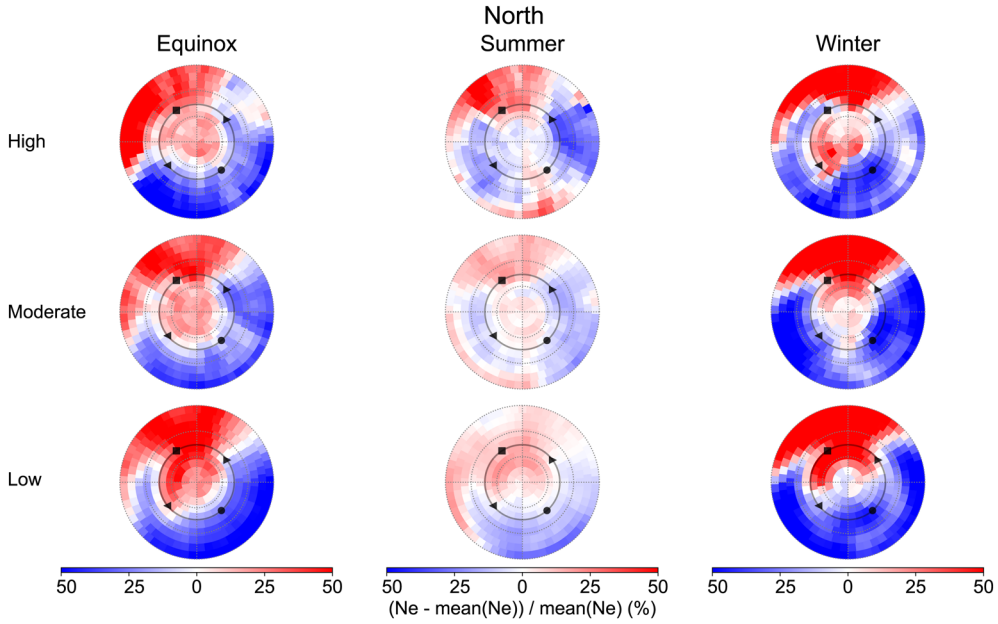

Figure 8. CHAMP/Swarm relative density maps in Modified Apex coordinates with a reference altitude of 110 km. The circle, right triangle, square, and left triangle respectively denote the location of the EISCAT Svalbard radar at 0, 6, 12, and 18 UT.

on the dayside at the lower latitudes seems consistent with diurnal variations of solar illumination. In the polar cap region, enhancement in the electron density can also be caused by transport of polar cap patches. At ESR latitudes, the largest enhancement is seen in the cusp region for most of the density maps.

4. Discussion

In Figures 6 and 7, it was shown that a depletion region typically occurs during the early morning hours above Svalbard. A decrease in the electron density during the early morning can also be seen in Figure 4 of Moen et al. (2008). Moen et al. (2008) studied the peak electron density using ESR data from two separate months (February 2001 and October 2002). In addition, Jones et al. (1990) observed a decrease in the electron density during early morning over 19–20 May 1987 when pointing the EISCAT Tromsø radar northwards. In the present study, we have used the database of accumulated ESR data to show that there is a statistical early morning electron density depletion region above Svalbard. These results have also been confirmed by space-based density measurements made by the Swarm and CHAMP satellites.

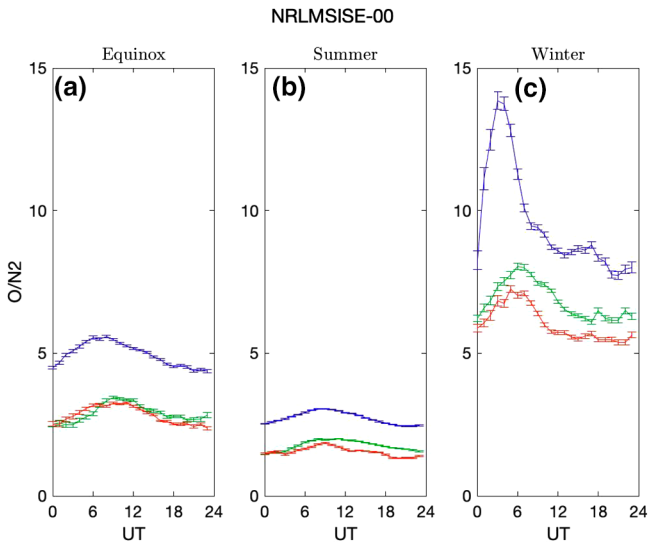

Figure 9. O/N_2 ratio from the NRLMSISE-00 model for equinox (left), summer (center), and winter (right). Each panel shows the O/N_2 ratio for three different levels of solar activity; high (red line), moderate (green line), and low (blue line).

In general, there are three main mechanisms that are known to cause such depletion regions. One of these mechanisms is connected to ion frictional heating and the other ones to prolonged recombination due to stagnation regions in the convection pattern or circulation in perpetual darkness. As shown in Figure 6, the post-midnight depletion region observed in the ESR data is usually colocated with an ion temperature enhancement. This might suggest that the formation of the depletion region observed in the ESR data is connected to frictional heating. Vanhamäki et al. (2016) and Voiculescu et al. (2016) observe an increase in the ion temperature colocated with a high-latitude post-midnight trough, and they suggest that ion frictional heating might play a part in the formation of the observed trough. Yamazaki et al. (2016) used ESR data from the

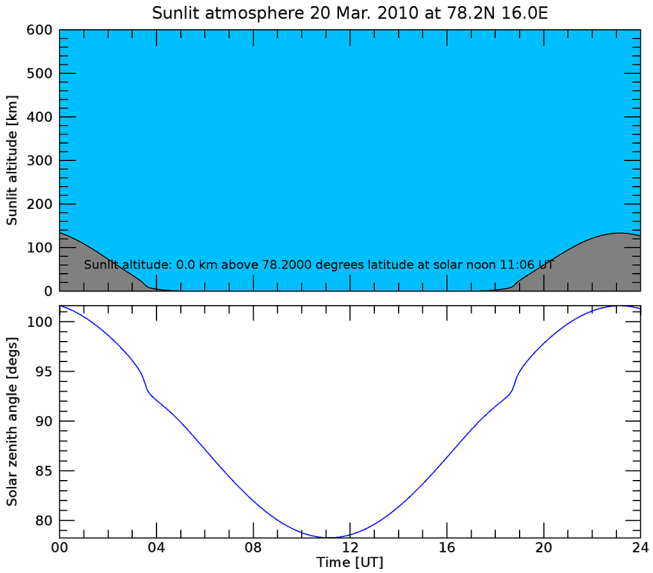

Figure 10. Sunlit atmosphere above Longyearbyen during spring equinox (top panel) and during winter solstice as a function of time of day (UT) for altitudes between 0 and 600 km. Solar zenith angle is shown in the bottom panel.

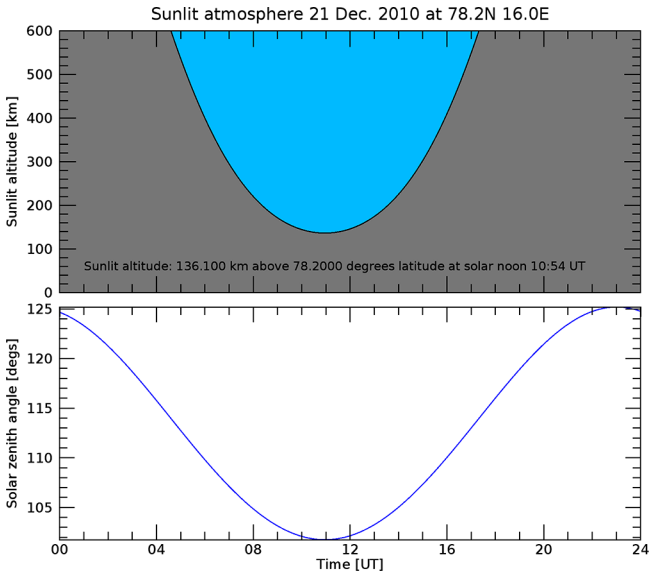

Figure 11. Sunlit atmosphere above Longyearbyen during winter solstice (top panel) as a function of time of day (UT) for altitudes between 0 and 600 km. Solar zenith angle is shown in the bottom panel.

solar minimum years 2007–2008 and found a pattern of ion temperature variations that is, similar to the pattern shown in Figure 6. Using TIE-GCM model simulations, they showed that the observed ion temperature enhancements are mainly caused by ion frictional heating. The occurrence of ion frictional heating is slightly higher during high solar activity (Davies et al., 1999), and it is therefore reasonable that we observe the early morning depletion region most clearly when the solar activity is high.

Ion frictional heating is the result of relative drift between ions and neutrals. The statistical distribution of thermospheric winds shows changes as a function of local time (e.g., Bjoland et al., 2015; Dhadly et al., 2019; Förster et al., 2008), and significant neutral winds exist at high latitudes. Strong neutral winds could also indicate that this is a region where frictional heating occur. A future study focusing on neutral winds and ion convection where electron density depletion is observed could further contribute to our understanding of the connection between frictional heating and electron density depletion.

The increased ion temperature co-located with the electron density depletion region could indicate that ion frictional heating is the mechanism responsible for this depletion region. However, Figure 6 indicates that in the early morning during summer, and in particular for low solar activity, the ion temperature reaches or is near its diurnal maximum while there is no clear indication of a corresponding depletion in electron density statistics. Thus, it is possible that several mechanisms could contribute to the formation of the depletion region.

In general, the early morning depletion region seems to be clearest during the equinox season and it is also more distinct during high solar activity than during low. Geomagnetic activity is known to have semiannual variations with peaks in the equinoxes and minima at the solstices, in addition to a strong solar cycle dependence (Rangarajan & Iyemori, 1997). These variations in the geomagnetic activity would also be expected to affect the electron density. However as solar cycle has a stronger effect on the geomagnetic activity level than season, and the depletion region could be seen clearly during all levels of solar activity during winter and equinox, it is unlikely that variations in geomagnetic activity could explain the seasonal and solar activity variations of the depletion region in Figures 6 and 7. These figures show that diurnal variations in general are smaller during summer than during the other seasons.

Another possible explanation to the seasonal and solar activity dependence is connected to thermospheric composition and temperature. Figure 9 shows the O/N_2 ratio calculated by running the NRLMSISE-00 model for the times where ESR data were available at 300 km altitude. The same seasonal and solar activity categories as in Figure 6 has also been used to make Figure 9. As shown, the O/N_2 ratio is lower for summer than for winter or equinox. However, during summer the O/N_2 ratio is higher for low solar activity than for high solar activity, and for low solar activity the summer O/N_2 ratio is comparable to the O/N_2 ratio in equinox during moderate or high solar activity. A higher O/N_2 ratio means that the chemical reaction rate of O^+ and N_2 is likewise relatively lower. The background ion temperature is also generally reduced during low solar activity and contributes to a decrease in the reaction rate between O^+ and N_2. It could therefore be possible that the formation of electron density depletion regions due to ion frictional heating is affected by the O/N_2 ratio and the background ion temperature, and this could explain the lack

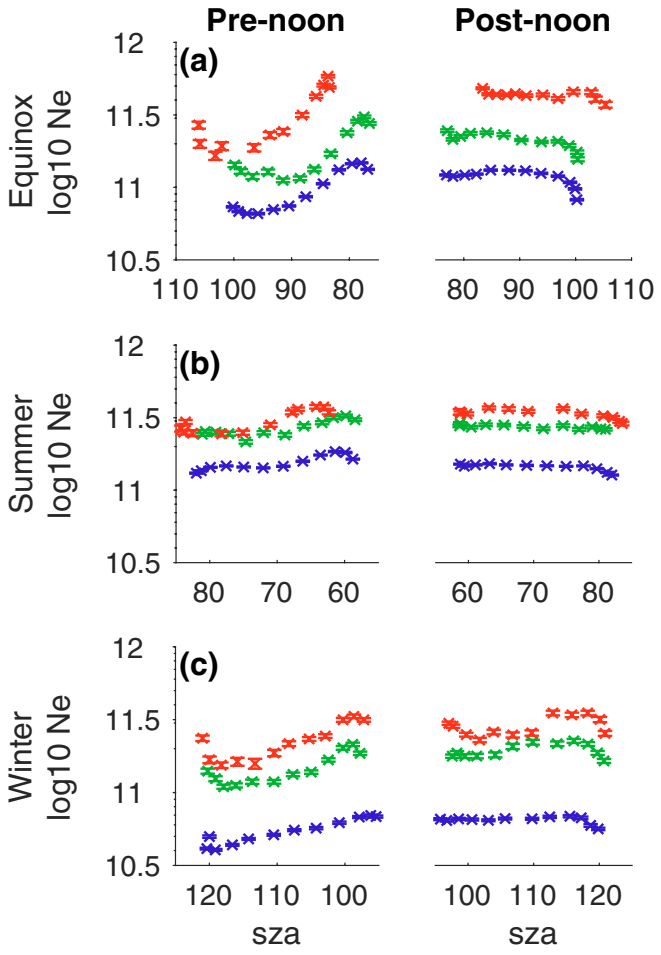

Figure 12. Plots of ESR electron density versus solar zenith angle for high (red), moderate (green), and low (blue) solar activity. The plots are divided into pre-solar noon (left) and post-solar noon (right). The rows show, from top to bottom, equinox, summer, and winter.

of the early morning electron density depletion region in summer for low solar activity. Future investigations using models would likely contribute to understanding these seasonal and solar activity variations.

In addition to ion frictional heating, stagnation regions in the convection pattern can also lead to electron density depletions. The convection pattern in the polar cap varies considerably with the orientation of the interplanetary magnetic field (IMF). In particular, during northward IMF convection cells which are entirely located inside the polar cap can exist. If this region is located in darkness, or if a stagnation region exists in a dark part of the convection pattern, depletion can occur due to recombination over a prolonged time period. However, above Svalbard, at 300 km altitude the ionosphere is sunlit during all 24 h of the day during summer and equinox (Figure 10). Only during winter (Figure 11) is the ionosphere in darkness during early morning. As the depletion region was observed to be clearest during equinox (Figure 6), it is unlikely that prolonged recombination in a dark part of the ionosphere is the main cause of the observed depletion region. Although both summer and equinox is sunlit, it is possible that the stronger solar production in summer compensate for plasma depletion caused by frictional heating, and this could therefore also be a possible explanation to the seasonal variations seen in Figures 6 and 7.

Although the mid-day *F*-region ionosphere above Svalbard is sunlit during most of the year, the solar zenith angle would still be expected to influence the electron density. To investigate if this effect is strong enough to suggest its role in the early morning depletion region, the hourly averaged electron densities from Figure 6 are plotted as a function of hourly averaged solar zenith angles in Figure 12. The same division into different categories of season and solar activity as in Figure 6 is used. In addition the data have been separated into a pre-noon and post-noon category as the dependence on solar zenith angle could be different in these two cases. Note that in Figure 12, "noon" refers to solar noon and not 12 UT. Figure 12 shows that the situation is different before and after solar noon. Pre-noon the electron density is typically lowest in the early morning when the solar zenith angle is high. After a few hours the electron density starts to increase, before it reaches its maximum 1–2 h before the solar zenith angle reaches its lowest value at local solar noon. Post-noon the curves are more flat and the electron density first starts to decrease in the evening. During equinox and winter there is a strong decrease in electron density when the solar zenith angles are larger than 100° and 115° respectively. This is likely an effect of solar production. During summer the decrease is much slower and starts at solar zenith angles above 80°. Results in Figure 12, indicate that it is unlikely that the early morning depletion region is caused solely by diurnal changes in solar illumination.

5. Summary and Conclusions

Measurements of electron density and ion temperature from the ESR have been used to study high-latitude depletion regions. The radars have been operational for several decades, and the accumulated database is a useful tool for studying seasonal, diurnal, geomagnetic and solar activity dependence of high-latitude electron density depletion regions. In this study the main goals have been to investigate the conditions under which electron density depletion regions occurs in the ESR data, and to understand the causes of these density depletion regions. Our results can be summarized as follows:

1. Electron density depletion regions are commonly observed in the early morning sector in both ESR data and Swarm and CHAMP data. Statistically, these regions are most pronounced during equinox and

winter under moderate to high solar activity. During summer, depletion regions occurs less frequently, appearing only during high solar activity in this study.

2. During equinox, the morning sector depletion regions for all three solar activity levels are coincident with an elevated ion temperature. During winter, there are well defined morning sector depletion regions for all three solar activity levels, but with varying levels of ion temperature, with no clear elevation during the depletion events. During summer, a well-defined morning sector depletion region occurs only during high solar activity level, although all three solar activity levels show elevated ion temperature in that sector.
3. There are three main mechanisms used to explain such depletion regions. Two of these mechanisms are related to prolonged recombination; either caused by a stagnation region in the convection pattern or by circulation in perpetual darkness. The last mechanism is connected to frictional heating. Our results indicate that it is unlikely that prolonged recombination is the only mechanism behind the observed depletion region. It is suggested that the formation is also connected to frictional heating and that this formation is affected by the background effective temperature, as well as seasonal and local time variations in the O/N_2 ratio and solar zenith angle.

Data Availability Statement

The Level 2 CHAMP PLP dataset and Level 1B Swarm LP dataset are publically accessible via ftp://isdcftp.gfz-potsdam.de and https://swarm-diss.eo.esa.int/, respectively. The *F*10.7 index is available via the NASA OMNI database (https://omniweb.gsfc.nasa.gov/form/dx1.html). All EISCAT radar data which we used in this study are provided in the web page of the EISCAT HQ:http://www.eiscat.se/schedule/schedule.cgi.

Acknowledgments
EISCAT is an international association supported by research organizations in China (CRIRP), Finland (SA), Japan (NIPR and STEL), Norway (NFR), Sweden (VR), and the United Kingdom (NERC).
This study was performed using database and internship program of National Institute of Polar Research (NIPR). Work at the Birkeland Center for Space Science and the University of Bergen was funded by the Research Council of Norway/CoE under contract 223252/F50 and by ESA contract 4000126731 in the framework of EO Science for Society

References

Aikio, A. T., Mursula, K., Buchert, S., Forme, F., Amm, O., Marklund, G., et al. (2004). Temporal evolution of two auroral arcs as measured by the Cluster satellite and coordinated ground-based instruments. *Annales Geophysicae*, *22*(12), 4089–4101. https://doi.org/10.5194/angeo-22-4089-2004

Benson, R. F., & Grebowsky, J. M. (2001). Extremely low ionospheric peak altitudes in the polar hole region. *Radio Science*, *36*(2), 277–285. https://doi.org/10.1029/1999RS002401

Bjoland, L. M., Chen, X., Jin, Y., Reimer, A. S., Skjæveland, Å., Wessel, M. R., et al. (2015). Interplanetary magnetic field and solar cycle dependence of Northern Hemisphere F region joule heating. *Journal of Geophysical Research: Space Physics*, *120*(2), 1478–1487. https://doi.org/10.1002/2014JA020586

Blelly, P.-L., Alcaydé, D., & van Eyken, A. P. (2010). A new analysis method for determining polar ionosphere and upper atmosphere characteristics from ESR data: Illustration with IPY period. *Journal of Geophysical Research*, *115*, A09322. https://doi.org/10.1029/2009JA014876

Brinton, H. C., Grebowsky, J. M., & Brace, L. H. (1978). The high-latitude winter F region at 300 km: Thermal plasma observations from AE-C. *Journal of Geophysical Research*, *83*(A10), 4767–4776. https://doi.org/10.1029/JA083iA10p04767

Buchau, J., Reinisch, B. W., Weber, E. J., & Moore, J. G. (1983). Structure and dynamics of the winter polar cap F region. *Radio Science*, *18*(6), 995–1010. https://doi.org/10.1029/RS018i006p00995

Buchert, S., Zangerl, F., Sust, M., André, M., Eriksson, A., Wahlund, J.-E., et al. (2015). SWARM observations of equatorial electron densities and topside GPS track losses. *Geophysical Research Letters*, *42*(7), 2088–2092. https://doi.org/10.1002/2015GL063121

Burns, A. G., Wang, W., Qian, L., Solomon, S. C., Zhang, Y., Paxton, L. J., et al. (2014). On the solar cycle variation of the winter anomaly. *Journal of Geophysical Research: Space Physics*, *119*(6), 4938–4949. https://doi.org/10.1002/2013JA019552

Carlson, H. C., Oksavik, K., Moen, J., van Eyken, A. P., & Guio, P. (2002). ESR mapping of polar-cap patches in the dark cusp. *Geophysical Research Letters*, *29*(10), 24-1–24-4. https://doi.org/10.1029/2001GL014087

Davies, J. A., Lester, M., & McCrea, I. W. (1999). Solar and seasonal dependence of ion frictional heating. *Annales Geophysicae*, *17*(5), 682–691. https://doi.org/10.1007/s00585-999-0682-4

Dhadly, M. S., Emmert, J. T., Drob, D. P., Conde, M. G., Aruliah, A., Doornbos, E., et al. (2019). HL-TWiM empirical model of high-latitude upper thermospheric winds. *Journal of Geophysical Research: Space Physics*, *124*(12), 10592–10618. https://doi.org/10.1029/2019JA027188

Doe, R. A., Mendillo, M., Vickrey, J. F., Zanetti, L. J., & Eastes, R. W. (1993). Observations of nightside auroral cavities. *Journal of Geophysical Research*, *98*(A1), 293–310. https://doi.org/10.1029/92JA02004

Förster, M., Haaland, S. E., Paschmann, G., Quinn, J. M., Torbert, R. B., Vaith, H., et al. (2008). High-latitude plasma convection during Northward IMF as derived from in-situ magnetospheric Cluster EDI measurements. *Annales Geophysicae*, *26*(9), 2685–2700. https://doi.org/10.5194/angeo-26-2685-2008

Friis-Christensen, E., Lühr, H., Knudsen, D., & Haagmans, R. (2008). Swarm – An Earth observation mission investigating geospace. *Advances in Space Research*, *41*(1), 210–216. https://doi.org/10.1016/j.asr.2006.10.008

Hatch, S. M., Haaland, S., Laundal, K. M., Moretto, T., Yau, A. W., Bjoland, L., et al. (2020). Seasonal and hemispheric asymmetries of F region polar cap plasma density: Swarm and CHAMP observations. *Journal of Geophysical Research: Space Physics*, *125*(11), e2020JA028084. https://doi.org/10.1029/2020JA028084

Jenner, L. A., Wood, A. G., Dorrian, G. D., Oksavik, K., Yeoman, T. K., Fogg, A. R., et al. (2020). Plasma density gradients at the edge of polar ionospheric holes: the absence of phase scintillation. *Annales Geophysicae*, *38*(2), 575–590. https://doi.org/10.5194/angeo-38-575-2020

Jones, G., Williams, P., Winser, K., & Lockwood, M. (1990). Characteristics of the high-latitude trough. *Advances in Space Research*, *10*(6), 191–196 https://doi.org/10.1016/0273-1177(90)90253-V

Kelley, M. C., Vickrey, J. F., Carlson, C. W., & Torbert, R. (1982). On the origin and spatial extent of high-latitude F region irregularities. *Journal of Geophysical Research*, *87*(A6), 4469–4475. https://doi.org/10.1029/JA087iA06p04469

Knudsen, D. J., Burchill, J. K., Buchert, S. C., Eriksson, A. I., Gill, R., Wahlund, J., et al. (2017). Thermal ion imagers and Langmuir probes in the Swarm electric field instruments. *Journal of Geophysical Research: Space Physics*, *122*(2), 2655–2673. https://doi.org/10.1002/2016JA022571

Kwagala, N. K., Oksavik, K., Lorentzen, D. A., Johnsen, M. G., & Laundal, K. M. (2018). Seasonal and solar cycle variations of thermally excited 630.0 nm emissions in the polar ionosphere. *Journal of Geophysical Research: Space Physics*, *123*(8), 7029–7039. https://doi.org/10.1029/2018JA025477

Laundal, K. M., & Richmond, A. D. (2016). Magnetic coordinate systems. *Space Science Reviews*, 1–33. https://doi.org/10.1007/s11214-016-0275-y

Lehtinen, M. S., & Huuskonen, A. (1996). General incoherent scatter analysis and GUISDAP. *Journal of Atmospheric and Solar-Terrestrial Physics*, *58*(1), 435–452. https://doi.org/10.1016/0021-9169(95)00047-X

Lomidze, L., Knudsen, D. J., Burchill, J., Kouznetsov, A., & Buchert, S. C. (2018). Calibration and validation of Swarm plasma densities and electron temperatures using ground-based radars and satellite radio occultation measurements. *Radio Science*, *53*(1), 15–36. https://doi.org/10.1002/2017RS006415

Ma, S. Y., Liu, P., & Schlegel, K. (2000). EISCAT observation of a high-latitude ionization trough associated with a reversed westward plasma flow. *Geophysical Research Letters*, *27*(20), 3269–3272. https://doi.org/10.1029/2000GL000073

McNamara, L. F., Cooke, D. L., Valladares, C. E., & Reinisch, B. W. (2007). Comparison of CHAMP and Digisonde plasma frequencies at Jicamarca, Peru. *Radio Science*, *42*(2). https://doi.org/10.1029/2006RS003491

Millward, G. H., Rishbeth, H., Fuller-Rowell, T. J., Aylward, A. D., Quegan, S., & Moffett, R. J. (1996). Ionospheric f 2 layer seasonal and semiannual variations. *Journal of Geophysical Research*, *101*(A3), 5149–5156. https://doi.org/10.1029/95JA03343

Moen, J., Qiu, X. C., Carlson, H. C., Fujii, R., & McCrea, I. W. (2008). On the diurnal variability in F2-region plasma density above the EISCAT Svalbard radar. *Annales Geophysicae*, *26*(8), 2427–2433. https://doi.org/10.5194/angeo-26-2427-2008

Oksavik, K., Barth, V. L., Moen, J., & Lester, M. (2010). On the entry and transit of high-density plasma across the polar cap. *Journal of Geophysical Research*, *115*(A12). https://doi.org/10.1029/2010JA015817

Oksavik, K., Ruohoniemi, J. M., Greenwald, R. A., Baker, J. B. H., Moen, J., Carlson, H. C., et al. (2006). Observations of isolated polar cap patches by the European Incoherent Scatter (EISCAT) Svalbard and Super Dual Auroral Radar Network (SuperDARN) Finland radars. *Journal of Geophysical Research*, *111*(A5), A05310. https://doi.org/10.1029/2005JA011400

Qian, L., Burns, A. G., Solomon, S. C., Wang, W., & Zhang, Y. (2016). Solar cycle variations of thermospheric composition at the solstices. *Journal of Geophysical: Research Space Physics*, *121*(4), 3740–3749. https://doi.org/10.1002/2016JA022390

Rangarajan, G. K., & Iyemori, T. (1997). Time variations of geomagnetic activity indices Kp and Ap: an update. *Annales Geophysicae*, *15*(10), 1271–1290. https://doi.org/10.1007/s00585-997-1271-z

Reigber, C., Lühr, H., Grunwaldt, L., Förste, C., König, R., Massmann, H., et al. (2006). CHAMP Mission 5 Years in Orbit. *Observation of the earth system from space* (pp. 3–15). Berlin: Springer-Verlag. https://doi.org/10.1007/3-540-29522-4_1

Richmond, A. D. (1995). Ionospheric electrodynamics using magnetic apex coordinates. *Journal of Geomagnetic and Geoelectricity*, *47*(2), 191–212. https://doi.org/10.5636/jgg.47.191

Rishbeth, H. (1998). How the thermospheric circulation affects the ionospheric F2-layer. *Journal of Atmospheric and Solar-Terrestrial Physics*, *60*(14), 1385–1402. https://doi.org/10.1016/S1364-6826(98)00062-5

Rodger, A., Moffett, R., & Quegan, S. (1992). The role of ion drift in the formation of ionisation troughs in the mid- and high-latitude ionosphere—a review. *Journal of Atmospheric and Solar-Terrestrial Physics*, *54*(1), 1–30. https://doi.org/10.1016/0021-9169(92)90082-V

Rother, M., Choi, S., Mai, W., Lühr, H., & Cooke, D. (2005). Status of the CHAMP ME data processing. *Earth observation with CHAMP results from three years in orbit* (pp. 413). https://doi.org/10.1007/3-540-26800-6_66

Russell, C. T., & McPherron, R. L. (1973). Semiannual variation of geomagnetic activity. *Journal of Geophysical Research*, *78*(1), 92–108. https://doi.org/10.1029/JA078i001p00092

Schunk, R. W., Banks, P. M., & Raitt, W. J. (1976). Effects of electric fields and other processes upon the nighttime high-latitude F layer. *Journal of Geophysical Research*, *81*(19), 3271–3282. https://doi.org/10.1029/JA081i019p03271

Sojka, J. J., Raitt, W. J., & Schunk, R. W. (1981). Plasma density features associated with strong convection in the winter high-latitude F region. *Journal of Geophysical Research*, *86*(A8), 6908–6916. https://doi.org/10.1029/JA086iA08p06908

Vanhamäki, H., Aikio, A., Voiculescu, M., Juusola, L., Nygrén, T., & Kuula, R. (2016). Electrodynamic structure of the morning high-latitude trough region. *Journal of Geophysical Research: Space Physics*, *121*(3), 2669–2682. https://doi.org/10.1002/2015JA022021

Vickers, H., Kosch, M. J., Sutton, E., Bjoland, L., Ogawa, Y., & La Hoz, C. (2014). A solar cycle of upper thermosphere density observations from the EISCAT Svalbard radar. *Journal of Geophysical Research: Space Physics*, *8*(8), 6833–6845. https://doi.org/10.1002/2014JA019885

Voiculescu, M., Nygrén, T., Aikio, A. T., Vanhamäki, H., & Pierrard, V. (2016). Postmidnight ionospheric troughs in summer at high latitudes. *Journal of Geophysical Research: Space Physics*, *121*(12), 12171–12185. https://doi.org/10.1002/2016JA023360

Williams, P., & Jain, A. (1986). Observations of the high latitude trough using EISCAT. *Journal of Atmospheric and Solar-Terrestrial Physics*, *48*(5), 423–434. https://doi.org/10.1016/0021-9169(86)90119-4

Winser, K., Jones, G., & Williams, P. (1986). A quantitative study of the high latitude ionospheric trough using EISCAT's common programmes. *Journal of Atmospheric Terrestrial Physics*, *48*(9), 893–904. https://doi.org/10.1016/0021-9169(86)90064-4

Yamazaki, Y., Kosch, M., Ogawa, Y., & Themens, D. (2016). High-latitude ion temperature climatology during the International Polar Year 2007-2008. *Journal of Space Weather and Space Climate*, *6*, A35. https://doi.org/10.1051/swsc/2016029

Zhang, S.-R., Holt, J. M., van Eyken, A. P., Heinselman, C., & McCready, M. (2010). IPY observations of ionospheric yearly variations from high- to middle-latitude incoherent scatter radars. *Journal of Geophysical Research*, *115*(A3). https://doi.org/10.1029/2009JA014327

Zhang, S.-R., Holt, J. M., van Eyken, A. P., McCready, M., Amory-Mazaudier, C., Fukao, S., et al. (2005). Ionospheric local model and climatology from long-term databases of multiple incoherent scatter radars. *Geophysical Research Letters*, *32*(20), L20102. https://doi.org/10.1029/2005GL023603

Zou, S., Moldwin, M. B., Nicolls, M. J., Ridley, A. J., Coster, A. J., Yizengaw, E., et al. (2013). Electrodynamics of the high-latitude trough: Its relationship with convection flows and field-aligned currents. *Journal of Geophysical Research: Space Physics*, *118*(5), 2565–2572. https://doi.org/10.1002/jgra.50120